Predictions and sensitivity forecasts for reionization-era [C ii] line intensity mapping

Sebastian Dumitru, Girish Kulkarni, Guilaine Lagache, Martin G. Haehnelt

Monthly Notices
of the
ROYAL ASTRONOMICAL SOCIETY

MNRAS **485,** 3486–3498 (2019)
Advance Access publication 2019 March 6

doi:10.1093/mnras/stz617

Predictions and sensitivity forecasts for reionization-era [C II] line intensity mapping

Sebastian Dumitru,[1,2,3] Girish Kulkarni ,[1,2,4★] Guilaine Lagache[5] and Martin G. Haehnelt[1,2]

[1]*Institute of Astronomy and Kavli Institute of Cosmology, University of Cambridge, Madingley Road, Cambridge CB3 0HA, UK*
[2]*Kavli Institute of Cosmology, University of Cambridge, Madingley Road, Cambridge CB3 0HA, UK*
[3]*Department of Physics and Astronomy, University of Pennsylvania, Philadelphia, PA 19104, USA*
[4]*Department of Theoretical Physics, Tata Institute of Fundamental Research, Homi Bhabha Road, Mumbai 400005, India*
[5]*LAM, Laboratoire d'Astrophysique de Marseille, CNRS, Aix Marseille Univ, Marseille, France*

Accepted 2019 February 27. Received 2019 February 19; in original form 2018 February 21

ABSTRACT

Observations of the high-redshift Universe using the 21 cm line of neutral hydrogen and complimentary emission lines from the first galaxies promise to open a new door for our understanding of the epoch of reionization. We present predictions for the [C II] 158 μm line and H I 21 cm emission from redshifts $z = 6$–9 using high-dynamic-range cosmological simulations combined with semi-analytical models. We find that the CONCERTO experiment should be able to marginally detect the large-scale power spectrum of [C II] emission to redshifts of up to $z = 8$ (signal-to-noise ratio $\sim$1 at $k < 0.1\ h\,\mathrm{cMpc}^{-1}$ with 1500 h of integration). A Stage II experiment similar to CCAT-p should be able to detect [C II] from even higher redshifts to high significance for similar integration times (signal-to-noise ratio of $\sim$50 at $k = 0.2\ h\,\mathrm{cMpc}^{-1}$ at $z = 6$). We study the possibility of combining such future [C II] measurements with 21 cm measurements using LOFAR and SKA to measure the [C II]−21cm cross power spectra, and find that a Stage II experiment should be able to measure the cross power spectrum for $k \lesssim 1\ h\,\mathrm{cMpc}^{-1}$ to signal-to-noise ratio of better than 10. We discuss the capability of such measurements to constrain astrophysical parameters relevant to reionization and show that a measurement of the [C II]−21cm cross power spectrum helps break the degeneracy between the mass and brightness of ionizing sources.

Key words: galaxies: high-redshift – intergalactic medium – dark ages, reionization, first stars.

1 INTRODUCTION

Atomic and molecular emission lines with wavelength redward of hydrogen Ly α have the desirable property of remaining visible deep into the epoch of hydrogen reionization (redshift $z = 6$–10), where the Ly α line is difficult to observe due to saturated absorption. These emission lines, which depend on the cold gas content, the ionizing radiation field, or the metallicity, uniquely probe the formation of the very first stars and galaxies. They should be a good tracer of the cosmic density structure.

Intensity mapping of such emission lines (e.g. O I, O III, C II, CO, H I, H_2) is an attractive tool to study the high-redshift Universe (Suginohara, Suginohara & Spergel 1999; Visbal & Loeb 2010; Carilli 2011; Gong et al. 2011; Lidz et al. 2011; Gong et al. 2012; Gong, Cooray & Santos 2013; Silva et al. 2015; Yue et al. 2015; Serra, Doré & Lagache 2016; Fonseca et al. 2017). By measuring large-scale variations in line emission from many individual unresolved galaxies, intensity mapping provides a statistical measurement that encodes cosmological and astrophysical information. This capacity of intensity mapping experiments is particularly important at redshifts corresponding to the epoch of reionization, which is a key period in the history of the Universe, when the earliest galaxies and quasars form and ionize the surrounding neutral hydrogen. Constraints from the evolution in the Ly α opacity of the intergalactic medium (IGM; e.g. Fan et al. 2006; Ota et al. 2017) and the temperature and polarization anisotropy in the cosmic microwave background (CMB; Planck Collaboration XLVII 2016) suggest that reionization occurs at redshifts $z \sim$ 6–15. However, the nature of the sources of reionization remains uncertain. Measurements of the escape fraction of Lyman-continuum photons necessary for reionization from high-redshift galaxies are still elusive. Although galaxies down to rest-frame UV magnitudes of $M_{\mathrm{UV}} = -12.5$ ($L \sim 10^{-3}L*$) at redshift $z = 6$ (Livermore, Finkelstein & Lotz

★ E-mail: kulkarni@theory.tifr.res.in

2017) and redshifts as high as $z = 11.1$ (Oesch et al. 2016) have been observed, the escape fraction of Lyman-continuum photons has been measured in only a handful of bright ($L > 0.5L*$) and low-redshift ($z < 4$) galaxies. In these galaxies, the escape fraction is typically found to be 2–20 per cent (Vanzella et al. 2010; Boutsia et al. 2011; Mostardi et al. 2015; Siana et al. 2015; Grazian et al. 2016; Japelj et al. 2017; Micheva et al. 2017) but reionization requires escape fractions of about 20 per cent in galaxies down to $M_{\rm UV} = -13$ (Robertson et al. 2015; Finkelstein 2016; Khaire et al. 2016). There is tentative evidence for a dominant contribution to reionization from quasars from the suggestion of a rather steep faint end of the QSO luminosity function at high redshift by Giallongo et al. (2015), and large Ly α opacity fluctuations at very large scales in QSO absorption spectra (Becker et al. 2015; Chardin et al. 2015; Davies & Furlanetto 2016). But it may be difficult to reconcile this with measurements of the He II Ly α opacity and measurements of the IGM temperature at $z \sim 3$ (Madau & Haardt 2015; D'Aloisio et al. 2017; Puchwein et al. 2019), and also with measurements of the incidence rate of metal-line systems (Finlator et al. 2016).

Intensity mapping of atomic and molecular lines emission from galaxies in the epoch of reionization has the potential to unambiguously reveal the properties of the sources of reionization. The radiative transfer of emission in these lines in galaxies is very different from that of the Lyman-continuum emission. As a result, intensity mapping yields a view of high-redshift galaxies that is unbiased by their Lyman-continuum escape fraction. Cross-correlating this measurement with a measurement of the ionization state of the large-scale IGM, such as of the 21 cm emission or absorption from the IGM, can then result in constraints on reionizing sources.

Several experiments are currently in deployment to measure the large-scale clustering in the 21 cm signal from the IGM during the epoch of reionization, such as Murchison Widefield Array (MWA; Bowman et al. 2013; Tingay et al. 2013), Low Frequency Array (LOFAR; van Haarlem et al. 2013; Pober et al. 2014), Hydrogen Epoch of Reionization Array (HERA; Pober et al. 2014, DeBoer et al. 2017), and Square Kilometre Array (SKA; astronomers.skatelescope.org). However, 21 cm power spectrum observations alone are limited in their capability of constraining reionization parameters. This is due to the degeneracy between the Lyman-continuum escape fraction (sometimes also parametrized as the ionization efficiency) and the mass of ionizing sources: a wide range in the host halo masses of ionizing sources can produce very similar large-scale 21 cm power for a variety of escape fraction values (Greig & Mesinger 2015). Cross-correlations with other line intensity maps can potentially solve this problem by breaking the degeneracy. Our aim in this paper is to investigate this possibility.

Various emission lines have been considered in the literature as candidates for high-redshift intensity mapping, such as Ly α (Silva et al. 2013; Pullen, Doré & Bock 2014), [O I] 63.2 and 145.5 μm (Visbal, Trac & Loeb 2011; Serra et al. 2016), CO(1–0) 2601 μm (Gong et al. 2011; Lidz et al. 2011), [N II] 121.9 and 205.2 μm (Serra et al. 2016), and [C II] 157.6 μm (Gong et al. 2012; Silva et al. 2015; Serra et al. 2016). As these lines are a result of a reprocessing of stellar emission by the interstellar medium (Barkana & Loeb 2001; Carilli & Walter 2013), we generally expect an anticorrelation on large scales between their signal and that of the 21cm line, which originates in the neutral regions far away from galaxies (Lidz et al. 2011). The intensity mapping technique has been used at $z \sim 0.8$ using the 21 cm line (Chang et al. 2010), and at $z \sim 3$ using the [C II] (Pullen et al. 2018) and CO (Keating et al. 2016) lines. Surveys suggested for future intensity mapping include CO Mapping Pathfinder (Li et al. 2016) for CO at redshifts $z \sim 2$–3; TIME (Crites et al. 2014) and CONCERTO (Serra et al. 2016; Lagache 2018) for [C II] at redshifts $z = 5$–9; HETDEX (Hill et al. 2008) for Ly α at $z = 1.9$–3.5; SPHEREx for Ly α at redshift $z \sim 6$–8 and other lines at lower redshifts (Doré et al. 2014, 2016), and CDIM (Cooray et al. 2016) for H α, O III, and Ly α at $z = 0.2$–10.

In this paper, we present predictions for [C II] and 21 cm brightness power spectra and the [C II]–21cm cross power spectra from the epoch of reionization ($z = 6$–10) using a high-dynamic-range cosmological hydrodynamical simulation from the Sherwood simulation suite (Bolton et al. 2017). We forecast the sensitivity to measure these statistical quantities for the CONCERTO experiment (Serra et al. 2016; Lagache 2018) as well as a Stage II successor experiment beyond TIME and CONCERTO for [C II]. For H I, we use the experimental set-ups of LOFAR and SKA. Finally, we discuss the feasibility of such experiments to constrain key parameters by considering simple models of reionization. The paper is organized as follows. We first present our [C II] emission-line model and 21 cm line maps in Sections 2 and 3, and then compute the cross-correlation between the [C II] and the 21 cm lines from the epoch of reionization in Section 4. We discuss the observability of the [C II] and 21 cm power spectra and the [C II]–21cm cross power spectrum in Section 5. Finally, we illustrate in Section 6 how the cross-correlation can be used to probe the nature of ionizing sources, using in particular two quantities: the minimum halo mass corresponding to a non-zero Lyman-continuum photon escape fraction and the number of ionizing photons produced by a halo. We end by summarizing our results in Section 7. Our ΛCDM cosmological model has $\Omega_{\rm b} = 0.0482$, $\Omega_{\rm m} = 0.308$, $\Omega_\Lambda = 0.692$, $h = 0.678$, $n = 0.961$, $\sigma_8 = 0.829$, and $Y_{\rm He} = 0.24$ (Planck Collaboration XVI 2014).

2 [C II] EMISSION FROM HIGH-REDSHIFT GALAXIES

We use a hydrodynamical cosmological simulation to model the [C II] and 21 cm signal from the epoch of reionization. This underlying simulation is identical to that used in previous work (Kulkarni et al. 2016, 2017), and is part of the Sherwood simulation suite (nottingham.ac.uk/astronomy/sherwood; Bolton et al. 2017). It has been run using the energy- and entropy-conserving TreePM smoothed particle hydrodynamical (SPH) code P-GADGET-3 that is derived from the publicly available GADGET-2 code (Springel, Yoshida & White 2001; Springel 2005). We perform this simulation in a periodic, cubic volume that is 160 h^{-1} cMpc long. A large dynamic range was achieved by using a softening length of $l_{\rm soft} = 3.13h^{-1}$ ckpc, and 2048^3 dark matter and gas particles. This results in a dark matter particle mass of $M_{\rm dm} = 3.44 \times 10^7$ $h^{-1}\,{\rm M}_\odot$ and gas particle mass of $M_{\rm gas} = 6.38 \times 10^6$ $h^{-1}\,{\rm M}_\odot$. Initial conditions were set-up at redshift $z = 99$ and evolved down to $z = 4$. We saved simulation snapshots at 40 Myr intervals between $z = 40$ and $z = 4$. In this paper, we use snapshots at $z = 6.3$, 7.1, 8.2, and 9. In order to speed the simulation up, galaxy formation is simplified by using the `QUICK_LYALPHA` implementation in P-GADGET-3. This converts gas particles with temperature less than 10^5 K and overdensity of more than a thousand times the mean baryon density to collisionless stars (Viel, Haehnelt & Springel 2004). Ionization and thermal state of the gas is derived by solving for the ionization chemistry under the assumption of an equilibrium with the metagalactic UV background modelled according to Haardt & Madau (2012). The UV background of Haardt & Madau (2012) is slightly modified to result in IGM temperatures that

agree with measurements by Becker et al. (2011). This chemistry solver assumes radiative cooling via two-body processes such as collisional excitation of H I, He I, and He II, collisional ionization of H I, He I, and He II, recombination, and bremsstrahlung (Katz, Weinberg & Hernquist 1996), and inverse Compton cooling off the CMB (Ikeuchi & Ostriker 1986). Metal enrichment and its effect on cooling rates is ignored. We identify dark matter haloes in the output snapshots using the friends-of-friends algorithm. In order to calculate power spectra, we project the relevant particles on to a grid to create a density field, using, in the case of gas particles, the cloud-in-cell (CIC) scheme that accounts for the SPH kernel.

If a source population at redshift z is assumed to have a line emission comoving volume emissivity $\varepsilon(\nu_{\rm obs}(1+z))$, then the specific intensity of the observed emission can be determined by solving the cosmological radiative transfer equation. The angle-averaged solution at $z=0$ can be written as

$$I(\nu_{\rm obs}, z=0) = \frac{1}{4\pi}\int_0^\infty {\rm d}z' \frac{{\rm d}l}{{\rm d}z'} \frac{\epsilon(\nu_{\rm obs}(1+z'))}{(1+z')^3}, \quad (1)$$

where ${\rm d}l/{\rm d}z = c/((1+z)H(z))$ denotes the proper line element, and we have assumed that there is negligible absorption by the intervening intergalactic medium. Assuming an absence of contamination from other redshifts, we can model the frequency dependence by a δ-function and write

$$I(\nu_{\rm obs}, z=0) = \frac{c}{4\pi}\frac{1}{H(z)}\frac{1}{\nu_{\rm em}(z)}\epsilon(\nu_{\rm obs}(1+z)), \quad (2)$$

where the $\nu_{\rm em} = \nu_{\rm obs}(1+z)$ is the rest-frame emission frequency.

The volume-averaged emissivity ε is related to the line luminosity L of individual haloes by

$$\epsilon(z) = \int_{M_{\rm min}}^\infty {\rm d}M \frac{{\rm d}n}{{\rm d}M} L_i(M, z), \quad (3)$$

where ${\rm d}n/{\rm d}M$ is the halo mass function. $M_{\rm min}$ is the minimum mass of haloes that can form stars and produce line emission. At $z=7$, the minimum halo mass in our simulation is $2.3\times10^8\ h^{-1}\,{\rm M}_\odot$, which is close to the atomic hydrogen cooling limit. The maximum halo mass at this redshift is $3.1\times10^{12}\ h^{-1}\,{\rm M}_\odot$. In order to model the emissivity $\varepsilon(z)$, we now need to model the halo luminosities $L(M, z)$.

2.1 Star formation rate

Linking the halo luminosities $L(M, z)$ to the star formation rate (SFR) can be done either using observational data or theoretical models of the emission processes of the different lines. The mechanism of line emission is complex; it depends on, e.g. the morphology and structure of galaxies, their metallicity, radiation field, and density. Line emission can be excited by starlight, dissipation of mechanical energy by turbulence and shocks, or by the active galactic nuclei. In the reionization epoch, CMB heating and attenuation can also be important (Lagache, Cousin & Chatzikos 2017). Several empirical models have been proposed for the emission of different lines, e.g. CO (Obreschkow et al. 2009; Gong et al. 2011), Ly α (Silva et al. 2013; Pullen et al. 2014; Feng, Cooray & Keating 2017), C II (Gong et al. 2012; Serra et al. 2016), but all of them rely on sets of poorly known parameters that characterize the galaxies and their interstellar medium in the reionization era. For the C II line, while individual galaxies have been detected at $z>6$ (e.g. Knudsen et al. 2016; Pentericci et al. 2016; Bradač et al. 2017; Carniani et al. 2017; Strandet et al. 2017), a complete understanding of the line excitation is still lacking.

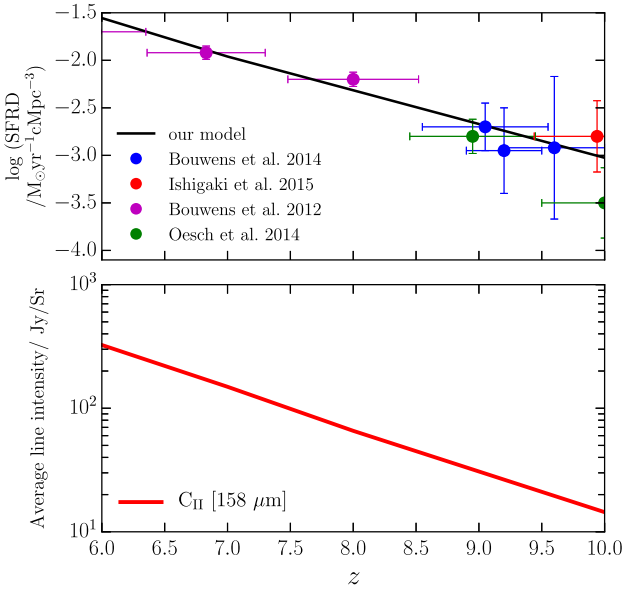

Figure 1. Top panel shows the SFR density evolution in our model (black curve) in comparison with various extinction-corrected observational measurements (coloured symbols). Bottom panel shows the resultant evolution of the average intensity of [C II] line emission.

Considering the large amount of uncertainties in the detailed modelling, we will continue our study using empirical relations from the literature that relate the halo luminosity to its SFR as a power law,

$$L_i \propto {\rm SFR}^\gamma, \quad (4)$$

where the exponent γ encodes possible non-linearities due to processes such as collisional excitation (Lagache et al. 2017). We assume that the SFR of a halo of mass M is proportional to the halo mass

$${\rm SFR} = f_*(z) M_{\rm halo}, \quad (5)$$

where we obtain the redshift-dependent proportionality factor by assuming a linear evolution of the log (SFRD) with redshift and calibrating $f_*(z)$ so that the resultant SFR density in the simulation box is consistent with observed data (Oesch et al. 2015). Fig. 1 shows the SFR density in our model in comparison with extinction-corrected observational measurements.

2.2 C II line emission

Once we have the SFR model, we assign [C II] line luminosities $L_{\rm [C\,II]}$ to each halo in our simulation box, by using the predicted $L_{\rm [C\,II]}$–SFR relation from the model presented by Lagache et al. (2017),

$$\log\left(\frac{L_{\rm [C\,II]}}{L_\odot}\right) = (1.4-0.07z)\times\log\left(\frac{\rm SFR}{{\rm M}_\odot{\rm yr}^{-1}}\right) + 7.1 - 0.07z. \quad (6)$$

In this paper, the semi-analytical model (SAM) of galaxy formation G.A.S. described in Cousin et al. (2015, 2016) was used, after further modifications assuming an inertial turbulent cascade in the gas that generates a delay between the accretion of the gas and the star formation (Cousin and Guillard, submitted). It is assumed that the [C II] emission in high-z galaxies arises predominantly

from photodominated regions (PDR). For each galaxy in the SAM, an equivalent PDR characterized by three parameters (the mean hydrogen density, gas metallicity, and interstellar radiation field) is defined. The [C II] line emission is then computed using the CLOUDY photoionization code (Ferland et al. 2017). This model allows computation of the [C II] luminosity for a large number of galaxies (e.g. 28 000 at $z = 5$). It takes into account the effects of CMB heating and attenuation that are important at such high redshifts. The model is able to reproduce the $L_{[C\,II]}$–SFR relation observed for 50 star-forming galaxies at $z \geq 4$. We used here the mean relation given in equation (6) although it is found that the $L_{[C\,II]}$–SFR relation is very dispersed (0.51–0.62 dex from $z = 7.6$ to $z = 4$). The large dispersion is due to the combined effect of different interstellar radiation fields, metallicities, and gas contents in the simulated high-redshift galaxies.

In order to calculate the three-dimensional distribution of the specific [C II] line intensity, we created coeval emission maps by assigning to each halo in the simulation volume a line luminosity $L_{[C\,II]}(M)$ modelled as above. Using the information about their spatial positions, we then sum the volume emissivities in each cell of a uniform 512^3 grid to obtain three-dimensional emission maps representing comoving regions of space of volume $(160\,\mathrm{cMpc}\,h^{-1})^3$. Using equation (2), the observed specific intensity corresponding to the cell is then given by

$$I_{\rm cell} = \frac{c}{4\pi}\frac{1}{\nu_{[C\,II]}H(z)}\frac{L_{[C\,II],\rm cell}}{V_{\rm cell}}, \tag{7}$$

where $L_{[C\,II],\rm cell}$ is the luminosity of the cell, given by the sum of the luminosities of any haloes located in the cell. Fig. 1 shows the evolution of the average line intensity. Fig. 2 shows a light cone of the [C II] specific intensity created by interpolating between simulation snapshots spaced at 40 Myr intervals between $z = 6$ and 10. The simulation corresponds to a total survey area of about 1.5 $\times$ 1.5 deg^2, with each cell occupying an area of 0.2 $\times$ 0.2 arcmin^2. At redshift $z = 7$, a comoving distance of 160 cMpc h^{-1} along the observation axis corresponds to about $\Delta z = 0.5$.

2.3 Power spectra

We derive three-dimensional spherically averaged power spectra of the [C II] line emission in our model as

$$\Delta^2(k) = \frac{k^3}{2\pi^2} \times \frac{\langle \widetilde{I}^2(k)\rangle}{V_{\rm box}}, \tag{8}$$

where $\widetilde{I}$ is the Fourier transform of the specific intensity defined in equation (2), and $V_{\rm box}$ is the box volume, $160\,\mathrm{cMpc}\,h^{-1})^3$. We ignore the anisotropies arising from redshift-space distortions and the redshift evolution across the box. Left column of Fig. 3 shows the resultant power spectra for the [C II] emission for redshifts from $z = 6$ to 9. The shot noise contribution to the [C II] power spectrum is included. The shot noise is given by

$$\Delta^2_{\rm shot}(k, z) = \frac{k^3}{2\pi^2}\left[\frac{c}{4\pi\,\nu_{[C\,II]}H(z)}\right]^2 \sum_i \frac{[L_{C\,II}(M_i, z)]^2}{V_{\rm box}}, \tag{9}$$

where $L_{C\,II}(M_i, z)$ is the C II luminosity (in erg s^{-1}) of halo i with mass M_i, and the summation is over all haloes. The frequency $\nu_{C\,II}$ is the rest-frame frequency of the C II line. Shot noise dominates the power spectrum at $k \gtrsim 0.5\ h\,\mathrm{cMpc}^{-1}$ (Serra et al. 2016), but is irrelevant in the [C II]−21cm cross power spectrum discussed in this paper, as the 21 cm emission comes from the extended IGM. Also shown in Fig. 3 are the sensitivities corresponding to experimental configurations, which we discuss below.

The line emission power spectra trace the halo power spectrum, with a constant bias factor as the emission amplitude is simply proportional to the halo mass. The amplitude of the [C II] power spectrum decreases from redshift $z = 6$ to 9 by a factor of 100. Our values are consistent with those from other models in the literature (Gong et al. 2012; Silva et al. 2015; Serra et al. 2016).

3 21 CM LINE MAPS

The redshifted 21 cm signal originates in the neutral intergalactic regions. We model the brightness temperature at location **x** in our simulations in a similar manner as Kulkarni et al. (2017)

$$T_b(\mathbf{x}) = \overline{T}_b x_{\rm H\,I}(\mathbf{x})\Delta(\mathbf{x}), \tag{10}$$

where the mean temperature $\overline{T}_b \approx 22\mathrm{mK}[(1+z)/7]^{1/2}$ (Choudhury, Haehnelt & Regan 2009), $x_{\rm H\,I}$ is the neutral hydrogen fraction in a cell, and Δ is the gas density in units of the average density in the simulation. We neglect the impact of redshift-space distortions due to peculiar velocities. We also assume that the spin temperature is much greater than the CMB temperature and that the Ly α coupling is sufficiently complete throughout the IGM.

We derive the ionization field by placing sources of Lyman-continuum radiation in dark matter haloes and using the well-known excursion set method (Furlanetto, Zaldarriaga & Hernquist 2004b; Choudhury et al. 2009; Mesinger, Furlanetto & Cen 2011). The total number of ionizing photons N_γ produced by a halo is assumed proportional to the halo mass (Kulkarni et al. 2016)

$$N_\gamma(M) = N_\gamma^{\rm LyC} M, \tag{11}$$

where the proportionality factor $N_\gamma^{\rm LyC}$ includes the Lyman-continuum escape fraction. A grid cell at position **x** is ionized if the condition

$$\langle n_\gamma(\mathbf{x})\rangle_R > \langle n_{\rm H}(\mathbf{x})\rangle_R(1+\bar{N}_{\rm rec}), \tag{12}$$

is satisfied in a spherical region centred on the cell for some radius R (Furlanetto, Zaldarriaga & Hernquist 2004a; Choudhury et al. 2009; Mesinger et al. 2011). Here, the averages are over the spherical region, $n_{\rm H}$ is the hydrogen number density,

$$n_\gamma = \int_{M_{\rm min}}^{\infty} {\rm d}M \left.\frac{{\rm d}N}{{\rm d}M}\right|_R N_\gamma(M), \tag{13}$$

where ${\rm d}N/{\rm d}M|_R$ is the halo mass function within the spherical region, $M_{\rm min}$ is the minimum halo mass that contributes ionizing photons, and $\bar{N}_{\rm rec}$ is the average number of recombinations per hydrogen atom in the IGM. The condition in equation (12) can be recast as

$$\zeta_{\rm eff}\, f(\mathbf{x}, R) \geq 1, \tag{14}$$

where the quantity

$$f = \rho_m(R)^{-1}\int_{M_{\rm min}}^{\infty} {\rm d}M \left.\frac{{\rm d}N}{{\rm d}M}\right|_R M, \tag{15}$$

is the collapsed fraction into haloes of mass $M > M_{\rm min}$, $M_{\rm min}$ is the minimum mass of haloes that emit Lyman-continuum photons, $\rho_m(R)$ is the average matter density, and ${\rm d}N/{\rm d}M|_R$ is the halo mass function in the sphere of radius R. The parameter $\zeta_{\rm eff}$ quantifies the number of photons in the IGM per hydrogen atom in stars, accounting for hydrogen recombinations in the IGM. We can write $\zeta_{\rm eff}$ in terms of the parameters of equations (11) and (12) as

$$\zeta_{\rm eff} = \frac{N_\gamma^{\rm LyC}}{1 - Y_{\rm He}}\left(1+\bar{N}_{\rm rec}\right)^{-1}, \tag{16}$$

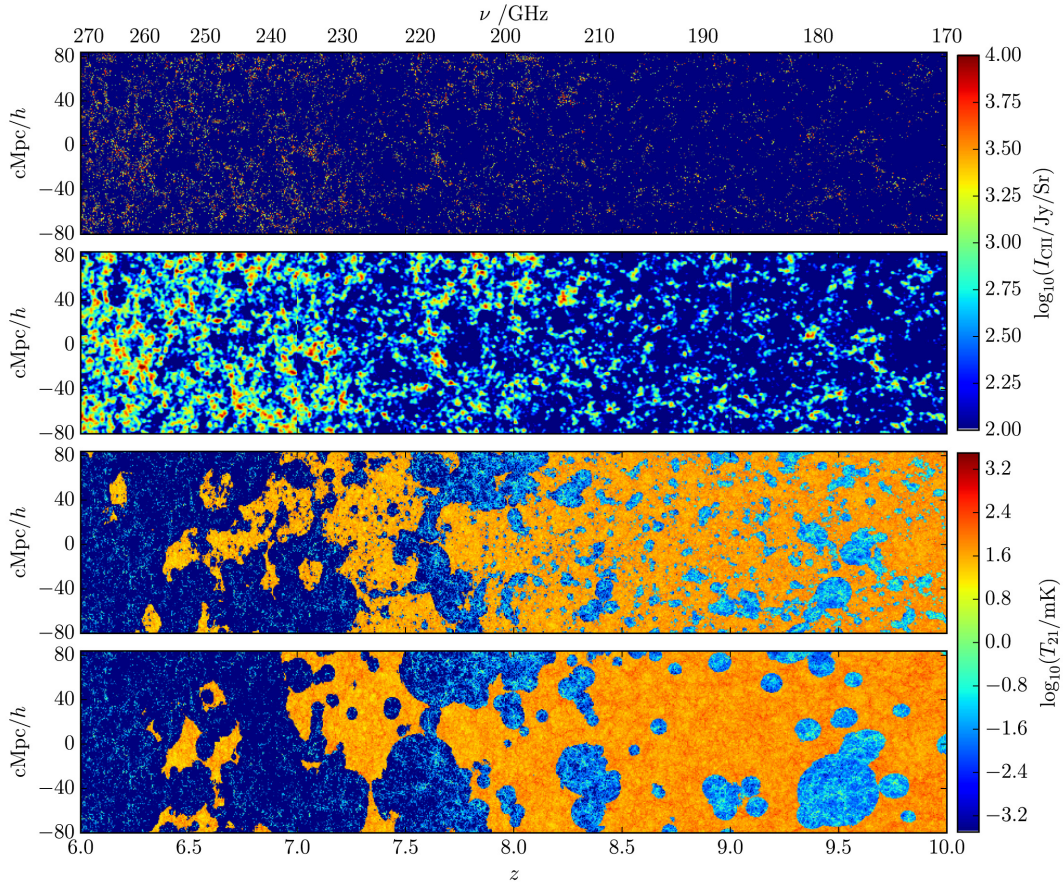

Figure 2. Light cones of [C II] and 21 cm brightness from redshift $z = 6$ to 10. The top panel shows individual sources corresponding to individual haloes with mass $M_{\rm min} = 10^8\,{\rm M}_\odot$; the bottom panel shows the [C II] intensity map with a resolution of 0.4 arcmin (∼1 cMpc at $z = 6$). The middle panel shows the 21 cm light cone in the reionization model with low-mass sources, while the bottom panel shows the 21 cm light cone in the reionization model with high-mass sources. The anticorrelation between the [C II] and 21 cm maps is visually apparent in the low-mass reionization model.

where $Y_{\rm He}$ is the helium mass fraction. This is the only parameter that determines the ionization field in this approach. The volume-weighted ionized fraction in the simulation box is $Q_V \equiv \sum_i Q_i/n_{\rm cell}$, where the ionized volume fraction in a cell i is Q_i and $n_{\rm cell}$ is the total number of grid cells.

We consider two reionization models in this paper. The evolution of the ionized fraction Q_V is identical in both models, and follows the evolution in the Late/Default model of Kulkarni et al. (2016). This is achieved by solving for $\zeta_{\rm eff}$ for the assumed Q_V. The simulation box is completely ionized, i.e. $Q_V = 1$, at $z = 6$. This evolution of the ionized fraction is consistent with the constraint from the CMB measurement of the electron scattering optical depth. The two models differ however in the range of halo masses that contribute to reionizing photons. In one of the models, we set the value of the minimum halo mass in equation (15) to be $M_{\rm min} = 2.3 \times 10^8\,{\rm M}_\odot$, which is approximately the mass of the smallest halo resolved in our simulation at $z = 7$. This model should represent reionization dominated by star-forming galaxies reasonably well. In our second reionization model, we assume $M_{\rm min} = 10^{11}\,{\rm M}_\odot$. Only high-mass haloes contribute to reionization in this model. These reionization models with low-mass and high-mass sources present two plausible but distinct cases of source clustering, which is the quantity of interest that we want to explore later in this paper by studying its effect on the 21 cm power spectrum and the [C II]−21cm cross power spectrum.

The bottom two panels of Fig. 2 show the evolution of 21 cm brightness in our two reionization models. These light cones are analogous to those obtained for the [C II] emission, shown in the top two panels of this figure. Although the average ionized hydrogen fraction is the same in the two reionization models, the distribution of the 21 cm signal is quite different. The reionization model with high-mass sources has large and more clustered ionized regions with low 21 cm brightness. More importantly, in the reionization model with low-mass sources, every source of [C II] emission is also a source of hydrogen-ionizing photons. As a result, the distribution of the 21 cm signal is anticorrelated with that of the [C II] signal: every [C II] source is located in regions with low 21 cm brightness. In the reionization model with high-mass sources, on the other hand, [C II] emitters in haloes with masses less than $M_{\rm min} = 10^{11}\,{\rm M}_\odot$ do not contribute any hydrogen-ionizing photons. As a result, these low-mass [C II] emitters are located in neutral regions, which are bright in 21 cm. This has an important effect on the [C II]−21cm correlation.

The middle columns of Figs 3 and 4 show the predicted 21 cm power spectra in our simulation in the reionization models with low-mass and high-mass sources, respectively. The power spectrum has a familiar shape: at small scales it is dominated by the matter power spectrum, and at large scales by a prominent 'bump' due to ionized bubbles. At $k = 0.1\ h\,{\rm cMpc}^{-1}$ the amplitude of the 21 cm power spectrum evolves from $\Delta^2(k) \sim 2\,{\rm mK}^2$ at $z = 9$ to $10\,{\rm mK}^2$ at $z = 7.1$

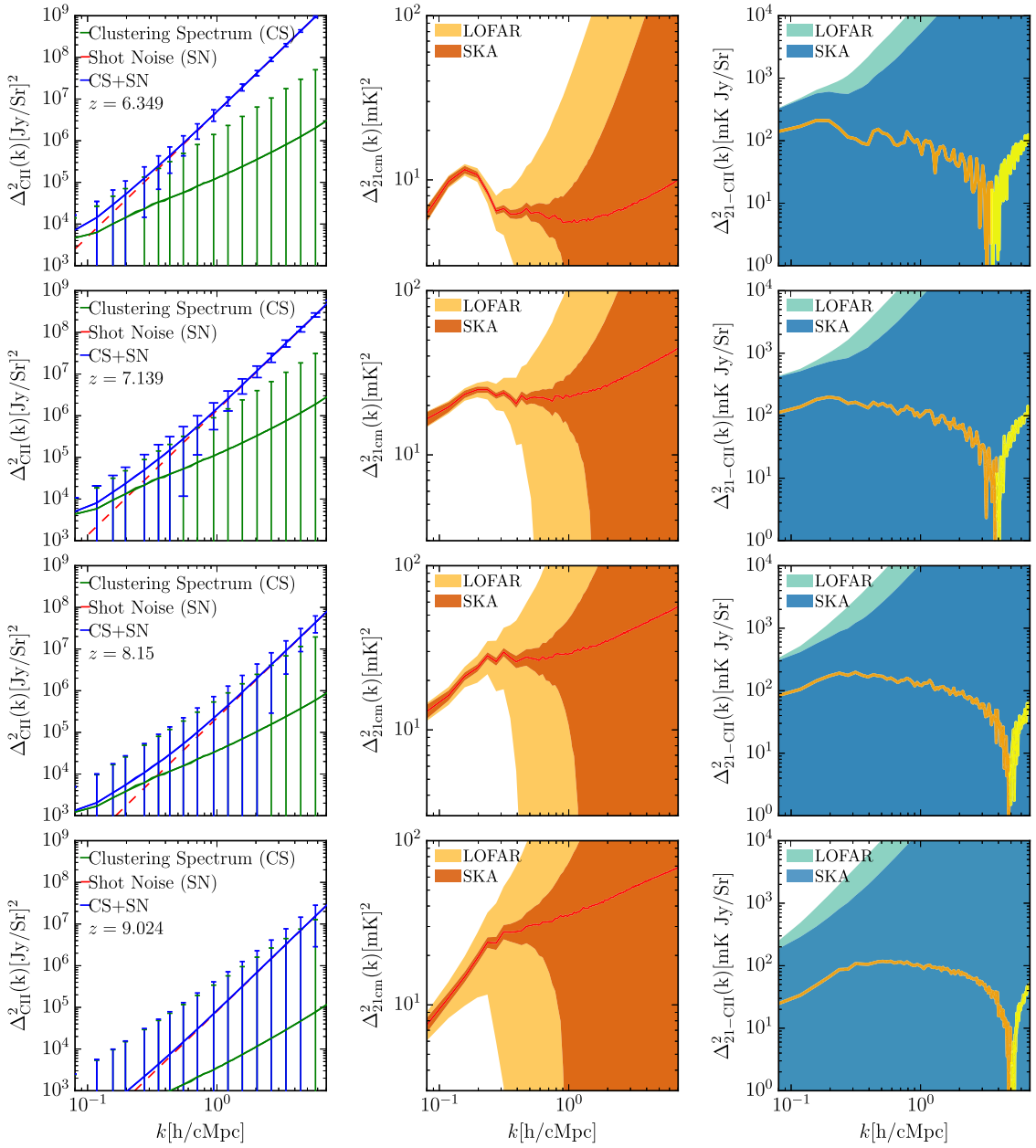

Figure 3. The [C II] power spectrum, 21 cm power spectrum, and [C II]−21cm cross power spectrum at redshifts $z = 6$–9 for the reionization model with low-mass sources. Red dashed and green solid curves in the left column show the shot noise and clustering contribution to the power spectrum, respectively. The blue curves in this column show the total power spectrum. Error bars on the [C II] power spectra show the 1σ sensitivities for CONCERTO for $\Delta z = 0.5$ at $z = 7$, relative to the total power spectrum in blue and relative to the clustering power spectrum in green. Two sets of shaded regions show errors corresponding to LOFAR and SKA1-LOW. On the cross power spectra on the right-hand panels, orange (yellow) lines are for negative (positive) cross-correlation coefficients.

in the reionization model with low-mass sources. In the high-mass case, the large-scale amplitude of the 21 cm power spectrum is higher, with $\Delta^2(k) \sim 35$ mK^2 at $z = 9$–30 mK^2 at $z = 7.1$, due to the higher clustering of ionized regions (Kulkarni et al. 2017). Figs 3 and 4 also show the sensitivity of experiments aiming to detect the 21 cm signal. We discuss this in Section 5 below.

4 THE [C II]−21CM CROSS POWER SPECTRUM

An exciting prospect for high-redshift [C II] intensity mapping is to combine it with observations of the coeval redshifted 21 cm line signal from the epoch of reionization. A detection of the [C II]−21cm cross power spectrum will assist in foreground decontamination and complement the [C II] and 21 cm power spectra as a probe of the epoch of reionization (Visbal & Loeb 2010; Lidz et al. 2011). Furthermore, the [C II]−21cm cross power spectrum may act as a direct tracer of the growth of ionizing bubbles during reionization (Gong et al. 2012).

As discussed above, Fig. 2 shows light cones of the [C II] and 21 cm intensity. Typically, on large scales, we expect the [C II] emission from haloes and the 21 cm signal from the IGM to be anticorrelated, because fully neutral regions do not contain emitting galaxies, while the halo-rich regions are depleted of neutral hydrogen. On scales smaller than the ionized bubbles, however,

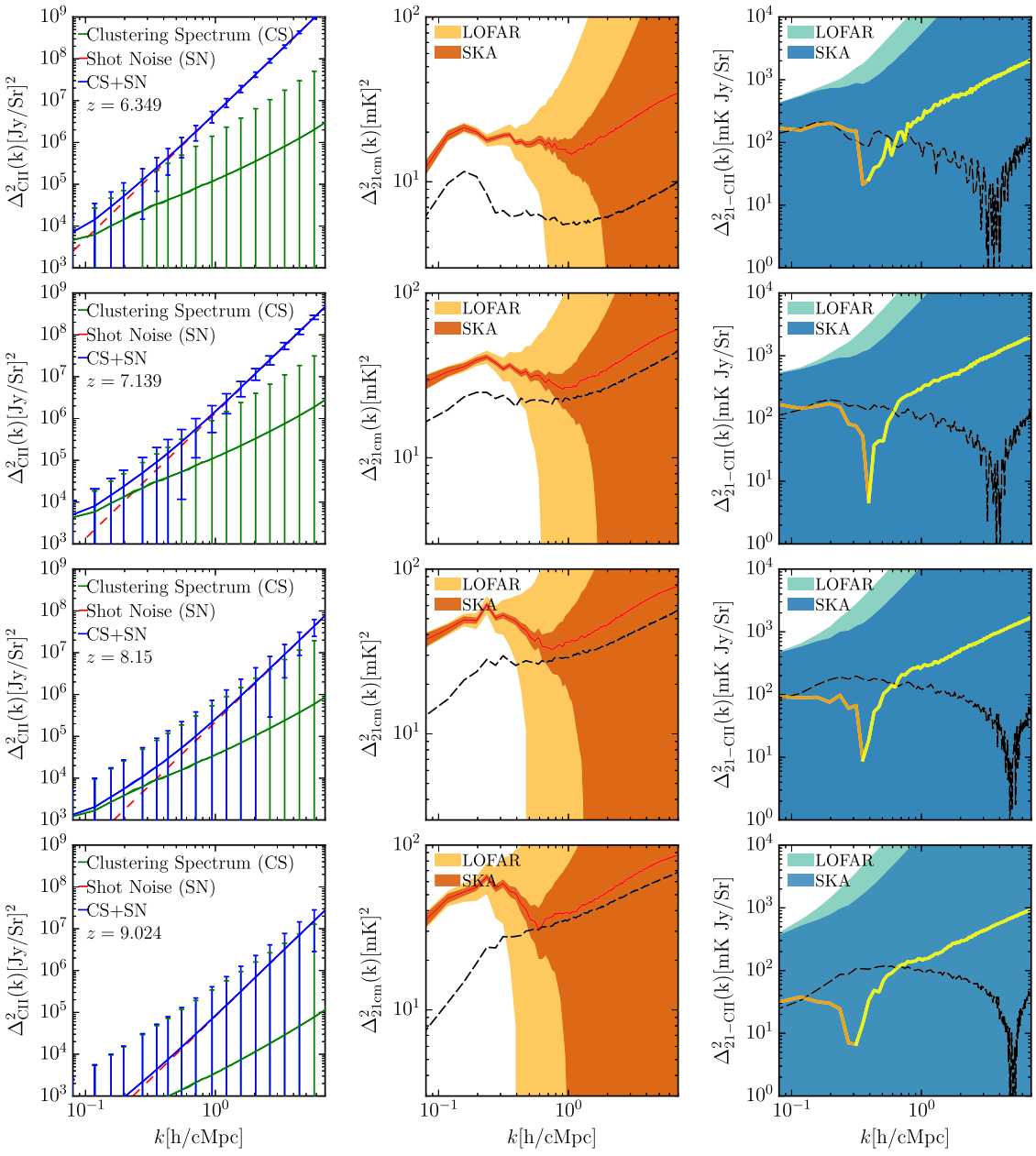

Figure 4. As Fig. 3 but for the reionization model with high-mass sources. The [C II] power spectra are identical to those in Fig. 3. The 21 cm power spectra and the [C II]−21cm cross power spectra from Fig. 3 are shown in dashed black for comparison.

there is positive correlation between the two fields. This behaviour is visually apparent in Fig. 2, particularly at redshift $z \sim 7$, where the ionized regions are sufficiently large.

In order to study this cross-correlation quantitatively, we define the cross power spectrum of the [C II] and 21 cm intensity maps as

$$\Delta^2(k) = \frac{k^3}{2\pi^2} \cdot \frac{1}{V_{\rm box}} \cdot \frac{\left\langle \widetilde{I}_1^{\,*}(k)\widetilde{I}_2(k) + \widetilde{I}_1(k)\widetilde{I}_2^{\,*}(k) \right\rangle}{2}, \qquad (17)$$

where I_1 and I_2 denote the intensities of [C II] and 21 cm, respectively. The quantity $\tilde{I}$ is the Fourier transform of I, and $\tilde{I}^*$ is the complex conjugate of $\tilde{I}$. The result is shown in the right column of Figs 3 and 4 for our reionization models with low-mass and high-mass sources, respectively. On large scales the cross-correlation is negative, as expected. In both models, at $k = 0.1\ h\,{\rm cMpc}^{-1}$, the value of the cross power spectrum is $\sim 10^2$ mK Jy sr^{-1} at redshift $z \sim 9$. This increases to close to 5×10^2 mK Jy sr^{-1} at $z \sim 6$. (Figs 3 and 4 also show the experimental sensitivities for measuring the cross power spectra; we discuss this in the next section).

The scale at which the cross power spectrum transitions from positive to negative values is quite different in the two reionization models. In the low-mass model, this scale is at $k_{\rm transition} = 3$–$5\ h\,{\rm cMpc}^{-1}$, while it is close to $k_{\rm transition} = 0.3\ h\,{\rm cMpc}^{-1}$ in the high-mass model. This is consistent with the picture that the transition scale measures the average size of ionized regions. As seen in Fig. 2, the ionized regions are larger in the high-mass model, which is reflected in the value of the transition scale of the cross power spectrum. Fig. 5 shows the evolution of the transition scale in the

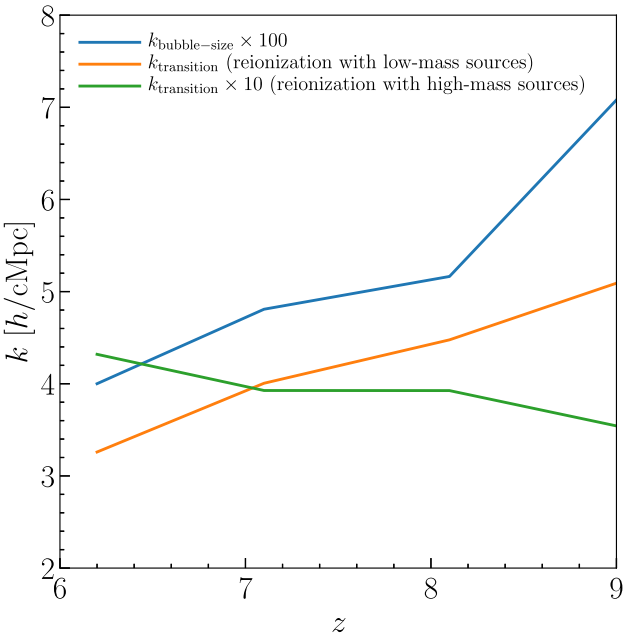

Figure 5. Evolution of the scale at which the [C II]−21cm cross power spectrum transitions from negative to positive values in the reionization model with low-mass sources (orange curve) and the reionization model with high-mass sources (green curve). The blue curve shows the evolution of the average ionized bubble size, defined simply at the cube root of the ionized volume in the simulation box. The transition scale tracks the bubble size evolution in the model with low-mass sources, but not in the model with high-mass sources. The quantities $k_{\rm bubble\ size}$ and $k_{\rm transition}$ for the high-mass reionization model have been multiplied by factors of 100 and 10, respectively, for easier comparison.

two models. The blue curve in this figure shows the evolution of the average bubble size $k_{\rm bubble\ size}$ in the simulation, as measured by the cube root of the ionized volume. The evolution of the cross power spectrum transition scale in the galaxy dominated model follows that of $k_{\rm bubble\ size}$, whereas the evolution in the transition scale for the high-mass model has a qualitatively different trend. This is because in the reionization model with low-mass sources, each [C II] source is also a source of hydrogen ionizing photons. Therefore, every [C II] source is in an ionized region, and there is perfect anticorrelation between the [C II] and 21 cm fields at scales larger than the bubble size. This is not the case in the high-mass reionization model, where most [C II] sources lie in neutral regions.

5 INTENSITY MAPPING EXPERIMENTS

To estimate the feasibility of [C II] intensity mapping, we consider the CONCERTO experiment (Serra et al. 2016; Lagache 2018). We also consider a successor Stage II experiment beyond CONCERTO. The specifications for these two experiments are summarized in Table 1. Our choice of the Stage II experiment parameters is inspired by the CCAT-p telescope.[1] For the 21 cm signal from the same redshifts, we consider measurements using LOFAR and SKA.

[1] www.ccatobservatory.org/docs/pdfs/Draft_CCAT-p.prospectus.170809.pdf.

Table 1. Specifications for [C II] experiments considered in this paper.

Parameter	CONCERTO	Stage II
Aperture size (D)	12 m	6 m
Transmission (T)	0.3	0.3
Frequency window ($\Delta\nu$)	80 GHz	80 GHz
Spectral resolution ($\delta\nu$)	1.5 GHz	0.4 GHz
NEI/$\sqrt{N_{\rm pix}}$	155 mJy s$^{1/2}$	31 mJy s$^{1/2}$
Survey area (A)	2 deg^2	10 deg^2
Survey duration ($t_{\rm survey}$)	1500 h	1000 h

5.1 [C II] experimental sensitivities

We estimate the sensitivity of experiments to measure the [C II] power spectrum by computing the uncertainty on the power spectrum following Lidz et al. (2011), Gong et al. (2012), and Serra et al. (2016):

$$\mathrm{var}[P_{\rm C\,II}(k)] = \frac{\left[P_{\rm C\,II}(k) + P^{\rm N}_{\rm C\,II}(k)\right]^2}{N_{\rm m}(k,z)}, \tag{18}$$

where $P_{\rm C\,II}(k)$ is the model power spectrum, $N_{\rm m}$ is the number of modes in the survey volume with wavenumber k at redshift z, and $P^{\rm N}_{\rm C\,II}$ is the noise power spectrum. The noise power spectrum is given by

$$P^{\rm N}_{\rm C\,II} = V_{\rm pix}\frac{\sigma^2_{\rm pix}}{t_{\rm pix}}, \tag{19}$$

where $V_{\rm pix}$ is the volume surveyed by a single pixel, $t_{\rm pix}$ is the observing time per pixel, and $\sigma^2_{\rm pix}$ is the noise variance per spectral element. The observing time per pixel is given by

$$t_{\rm pix} = t_{\rm survey} N_{\rm pix}\frac{\Omega_{\rm beam}}{A}. \tag{20}$$

Here, $t_{\rm survey}$ is the survey duration, which we take to be 1500 h. The beam area $\Omega_{\rm beam}$ is given by $\Omega_{\rm beam} = 2\pi(\theta_{\rm beam}/2.355)^2$, where $\theta_{\rm beam} = 1.22\lambda_{\rm obs}/D$ and $D = 12$ m for CONCERTO. We assume a survey area of $A = 2$ deg^2. The volume surveyed by one pixel is given by (Gong et al. 2012)

$$V_{\rm pixel}(z) = 1.1\times10^3(\mathrm{cMpc}\,h^{-1})^3\left(\frac{\lambda}{158\ \mu\mathrm{m}}\right)\times\left(\frac{1+z}{8}\right)^{1/2}\left(\frac{\theta_{\rm beam}}{10\ \mathrm{arcmin}}\right)^2\left(\frac{\delta\nu}{400\ \mathrm{MHz}}\right). \tag{21}$$

The noise variance $\sigma^2_{\rm pix}$ in equation (19) is given by

$$\sigma^2_{\rm pix} = \frac{\mathrm{NEI}^2_{\rm diff}}{N_{\rm pix}}, \tag{22}$$

where the noise equivalent power input from diffuse emission, defined as the power from diffuse emission absorbed that produces a signal-to-noise ratio of unity at detector output, is (in MJy sr^{-1} s$^{1/2}$)

$$\mathrm{NEI}_{\rm diff} = \mathrm{NEI}\times\frac{10^{-9}}{\Omega_{\rm beam}}. \tag{23}$$

For CONCERTO, NEI/$\sqrt{N_{\rm pix}} = 155$ mJy s$^{1/2}$ (see table 3 of Serra et al. 2016), assuming an overall transmission of the system $T = 0.3$, a spectral resolution $\delta\nu = 1.5$ GHz, a number of pixel (and thus of spectrometer) $N_{\rm pix} = 1500$, a precipitable water vapour of 2 mm, an elevation of 60 deg, and assuming the sensitivity already achieved by the NIKA2 KIDS detectors on sky (Adam et al. 2018).

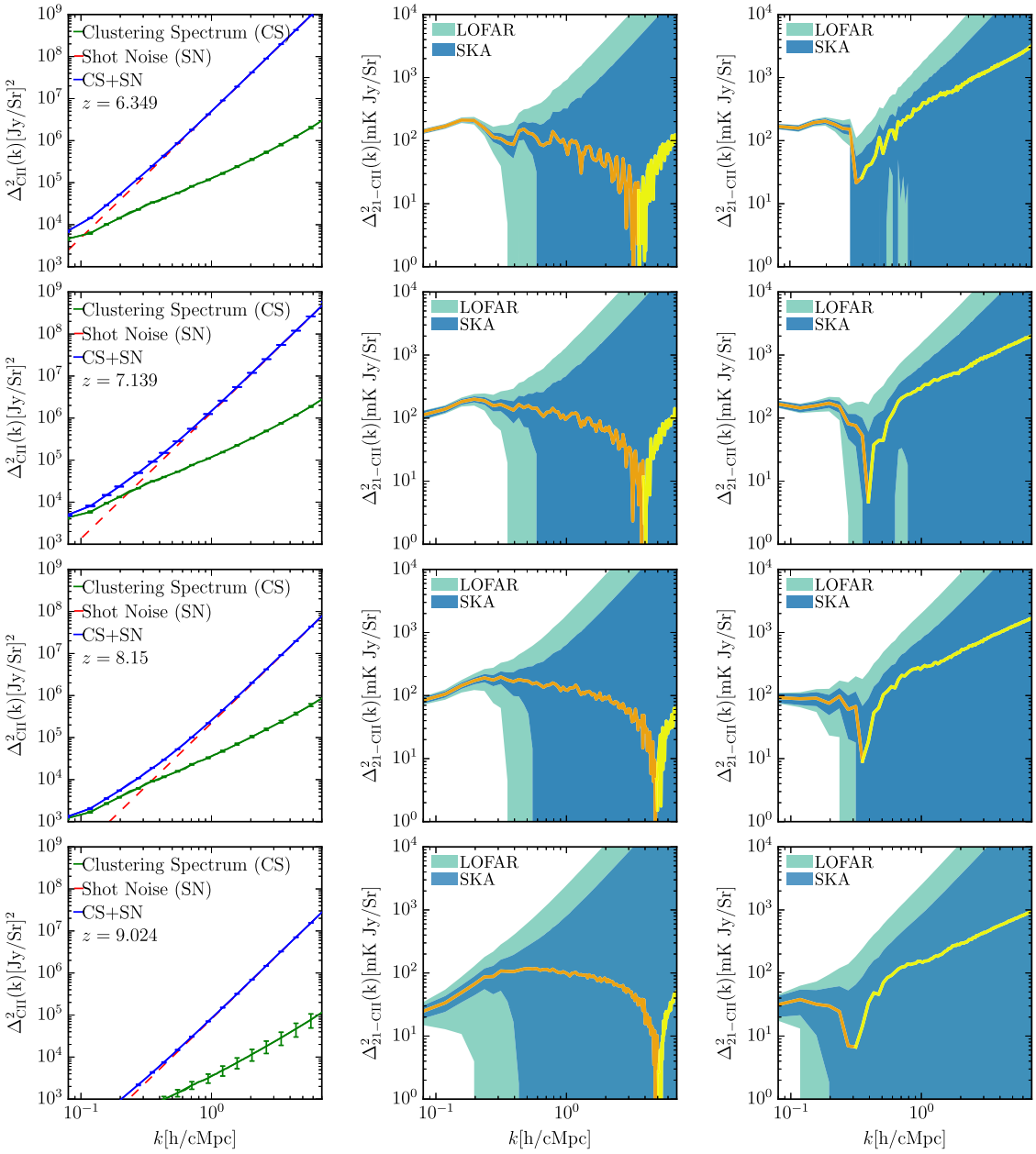

Figure 6. The [C II] power spectrum, and the [C II]−21 cm cross power spectrum for reionization models with low-mass and high-mass sources at redshifts $z = 6$–9. Errorbars on the [C II] power spectra show sensivities for the Stage II experiment assuming a survey area of 10 deg^2 and integration time of 1000 h. Two sets of shaded regions on the cross power spectra show errors corresponding to LOFAR and SKA surveys.

The number of Fourier modes $N_{\rm m}$ in equation (18) is given by

$$N_{\rm m}(k, z) = 2\pi k^2 \Delta k \frac{V_{\rm survey}}{(2\pi)^3}. \quad (24)$$

Here, Δk is the bin size assumed in k space, and the survey volume is given by

$$V_{\rm survey}(z) = 3.7 \times 10^7 ({\rm cMpc}\, h^{-1})^3 \left(\frac{\lambda}{158\,\mu{\rm m}}\right) \times \left(\frac{1+z}{8}\right)^{1/2} \left(\frac{A}{16\,{\rm deg}^2}\right) \left(\frac{B_\nu}{20\,{\rm GHz}}\right). \quad (25)$$

This allows us to estimate var$[P_{\rm C\,II}(k)]$ using equation (18). (Note that equation 24 is approximate and may lead to an overestimated signal-to-noise ratio). Table 1 summarizes all the properties of the CONCERTO experiment.

The left columns in Figs 3 and 4 show the uncertainties in the [C II] power spectrum for the CONCERTO experiment from $z \sim 6$ to $\sim$9. We find that the CONCERTO should be able to measure the large-scale power spectrum of [C II] emission to redshifts of up to $z = 8$ (with a signal-to-noise ratio of $\sim$1 at $k < 0.1\ h\,{\rm cMpc}^{-1}$ with 1500 h of integration). Our predictions thus agree with the 'pessimistic' case discussed by Lagache (2018).

For the Stage II experiment, we consider a noise equivalent flux density (NEFD) that is five times better than CONCERTO. We assume an aperture size of $D = 6$ m, and a spectral resolution of $\delta\nu = 400$ MHz. The survey duration is assumed to be $t_{\rm survey} = 1000$ h, while the survey area is set to $A = 10$ deg^2. These

Table 2. Specifications for 21 cm experiments considered in this paper. We use SKA parameters obtained by Ghara, Choudhury & Datta (2016) which broadly agrees with the baseline distribution given in the latest SKA1-LOW configuration document (Document number SKA-SCI-LOW-001; date 2015-10-28; http://astronomers.skatelescope.org/documents/).

Parameter	LOFAR	SKA1-LOW
Number of antennae ($N_{\rm ant}$)	48	512
Effective collecting area ($A_{\rm eff}$)	526.0 m^2	962.0 m^2
Maximum baseline ($b_{\rm max}$)	3475.6 m	40286.8 m
Minimum baseline ($b_{\rm min}$)	22.92 m	16.8 m
Survey duration per day ($t_{\rm per\ day}$)	6 h	6 h
Survey number of days	120	120
System temperature ($T_{\rm sys}$)	Equation (28)	Equation (28)

parameters are also summarized in Table 1. The left columns in Fig. 6 shows the uncertainties in the [C II] power spectrum for the Stage II experiment from $z \sim 6$ to 9. The signal-to-noise ratio is now enhanced by a factor of ∼40 relative to CONCERTO at $k = 0.2\,h\,{\rm cMpc}^{-1}$ at $z = 6$. With the Stage II experiment, the power spectrum is detectable even at $z \sim 9$ with a signal-to-noise ratio of ∼50 at $k = 0.2\,h\,{\rm cMpc}^{-1}$.

5.2 21 cm experimental sensitivities

We study here the detectability of the 21 cm power spectrum for LOFAR (van Haarlem et al. 2013) and the low-frequency instrument from Phase 1 of the SKA1-LOW (astronomers.skatelescope.org). These are listed in Table 2. Similar to equation (18), the variance of the power spectrum at mode k and redshift z is given by

$$\mathrm{var}[P_{21}(k)] = \frac{\left[P_{21}(k) + P_{21}^{\rm N}(k)\right]^2}{N_{\rm m}(k,z)}. \tag{26}$$

The noise power spectrum $P_{21}^{\rm N}(k)$ is estimated similar to Parsons et al. (2012), and is given by

$$P_{21}^{\rm N}(k) \approx X^2 Y \frac{k^{-1/2}}{2\pi^2}\left(\frac{1}{B}\right)^{1/2}\left(\frac{1}{\Delta \ln k}\right)^{1/2} \times \frac{\Omega}{2t}T_{\rm sys}^2\frac{u_{\rm max}^{1/2}}{N}\frac{1}{\Omega^{1/4}}\frac{1}{t_{\rm per\,day}^{1/2}}, \tag{27}$$

where $u_{\rm max}$ is the maximum baseline $b_{\rm max}$ in wavelength units, and X and Y are conversion factors from angles and frequencies, respectively, to comoving distance (see Kulkarni et al. 2016 for further details). We assume $t_{\rm per\ day} = 6$ h for 120 d. Also in equation (27), N is the number of baselines and Ω is the field of view of an element in the array. The system temperature is assumed to be Thompson, Moran & Swenson (2007)

$$T_{\rm sys} = 60\,{\rm K}\left(\frac{300\,{\rm MHz}}{\nu_c}\right)^{2.25}, \tag{28}$$

and calculate the thermal noise power for an integration over 120 d, assuming a bandwidth of 6 MHz, an observing time of 6 h per day for 120 d, and a mid-latitude location.

The middle columns of Figs 3 and 4, show the resultant uncertainties in the 21 cm power spectrum for LOFAR (yellow) and SKA (brown). These experiments are only sensitive to large scales due to limited baselines. Neither of the experiments are sensitive to 21 cm power for $k \gtrsim 1\ {\rm cMpc}^{-1}h$. SKA1-LOW has much greater sensitivity than LOFAR primarily due to large number of antenna elements. The signal-to-noise ratio is about 100 for these two experiments $k \sim 0.1\ {\rm cMpc}^{-1}h$. LOFAR has sensitivity for scales corresponding to $k \lesssim 0.2\ {\rm cMpc}^{-1}h$. At $k \sim 0.1\ {\rm cMpc}^{-1}h$, the signal-to-noise ratio for LOFAR is ∼10.

5.3 C II−21cm cross power spectrum sensitivity

We calculate the uncertainty on the cross power spectrum of [C II] with 21 cm following Gong et al. (2012),

$$\mathrm{var}[P_{\rm C\,II,21}(k,z)] = \frac{1}{2}\left[\frac{P_{21,\rm C\,II}^2 + P_{21}^{\rm total}(k,z)P_{\rm C\,II}^{\rm total}}{N_{\rm m}(k,z)}\right], \tag{29}$$

where

$$P_{21}^{\rm total}(k,z) = P_{21}(k,z) + P_{21}^{\rm N}(k,z), \tag{30}$$

and

$$P_{\rm C\,II}^{\rm total}(k,z) = P_{\rm C\,II}(k,z) + P_{\rm C\,II}^{\rm N}(k,z). \tag{31}$$

The right-hand side columns in Figs 3 and 4 show the errors on the cross power spectra for CONCERTO-LOFAR (cyan) and CONCERTO-SKA (blue) combinations. In both cases, a high-signal-to-noise detection of the cross power spectrum is unlikely at least for scales smaller than $k \sim 0.1\ {\rm cMpc}^{-1}h$ at $z = 6$–9. In the reionization model with low-mass sources, the transition scale at which the cross power spectrum changes sign is at $k \sim 5\ {\rm cMpc}^{-1}h$, which is out of the experimental reach. However, as discussed in the previous section, the transition scale is much larger, $k \sim 0.3\ {\rm cMpc}^{-1}h$, in the case of reionization by high-mass sources. This allows a detection of this scale, at least at redshifts $z = 6$ and 7. Fig. 6 shows errors on the cross power spectra for LOFAR (cyan) and SKA (blue) combined with our Stage II [C II] experiment. As expected the sensivities are enhanced now to scales $k \sim 5\ {\rm cMpc}^{-1}h$ for LOFAR and $k > 6\ {\rm cMpc}^{-1}h$ for SKA at $z = 7$. Note that as the 21 cm signal originates in the extended IGM, the shot noise contribution to the 21 cm power spectrum and the [C II]−21cm cross power spectrum is subdominant (Kulkarni et al. 2016) and is not computed here.

6 FORECASTS FOR CONSTRAINTS

We now consider the constraints that can be obtained for astrophysical parameters related to reionization from measurements of (i) the 21 cm power spectrum alone, and (ii) the 21 cm power spectrum and the [C II]−21cm cross power spectrum. A variety of astrophysical parameters determine the [C II] and 21 cm emission from the high-redshift Universe. As such [C II] and 21 cm experiments can potentially constrain all of these. However, for simplicity, we consider only two parameters. We consider a scenario in which haloes down to the mass corresponding to the atomic hydrogen cooling limit $T_{\rm vir} = 10^4$ K produce [C II] emission, but only haloes with mass $M > M_{\rm esc}$ have a non-zero Lyman-continuum photon escape fraction. Our simulation resolves haloes close to the atomic hydrogen cooling limit. Thus, this scenario assumes that all haloes in our simulation are able to produce [C II] emission, but only massive haloes with mass $M > M_{\rm esc}$ participate in reionization of the IGM. The second parameter of our model is $N_\gamma^{\rm LyC}$, which appears in equation (11) and sets number N_γ of ionizing photons produced by a halo. Our two parameters, $M_{\rm esc}$ and $N_\gamma^{\rm LyC}$ thus set the minimum mass of haloes that produce ionizing photons and their Lyman-continuum brightness, respectively. The dependence of the Lyman-continuum photon escape fraction on the halo mass is not well understood. Our choice of these parameters is therefore a simple

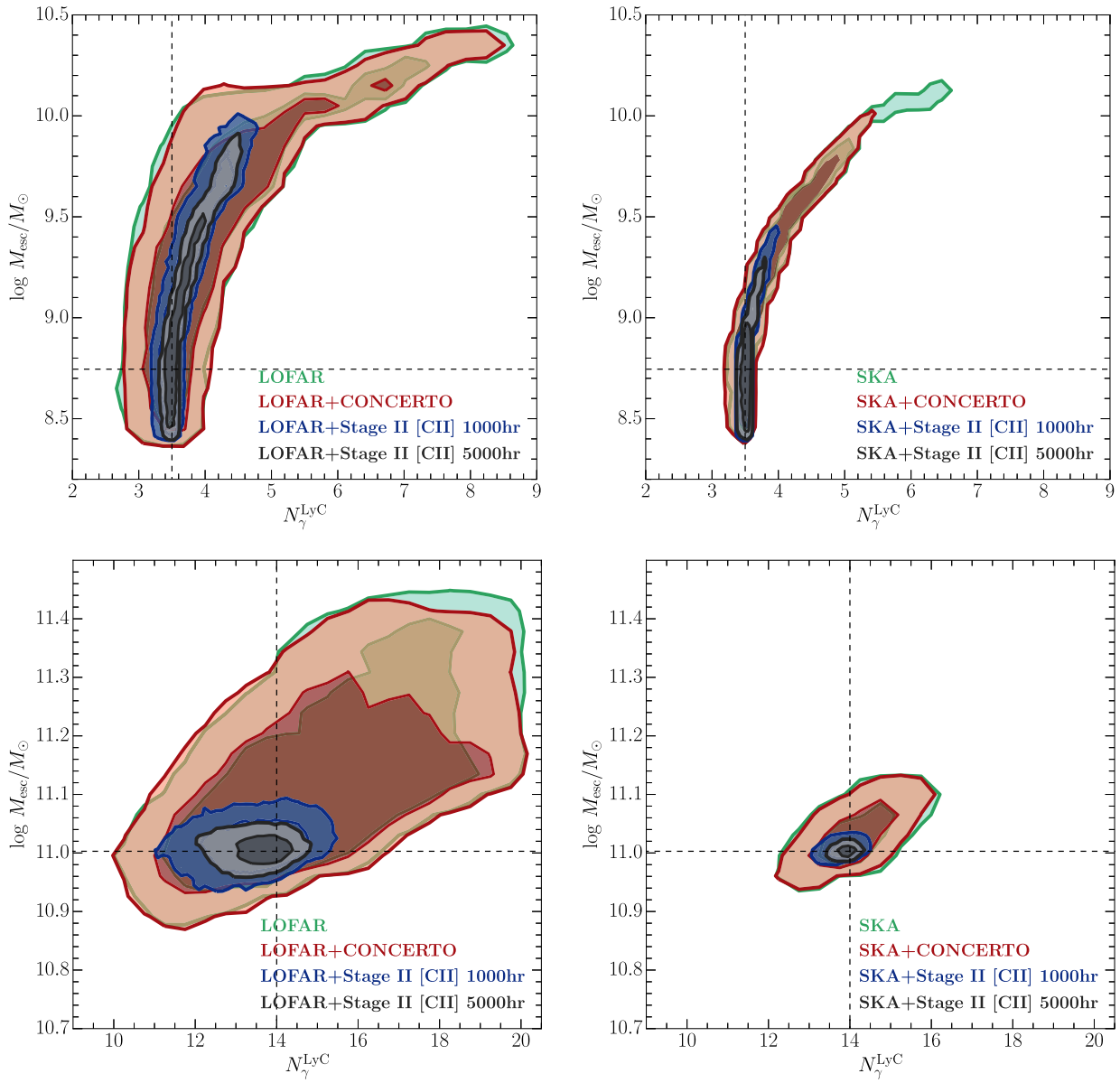

Figure 7. Constraints on astrophysical parameters from mock measurements of the 21 cm power spectrum and the [C II]−21cm cross power spectrum. Panels in the top row describe the reionization scenario with low-mass sources, and those in the bottom row describe the reionization scenario with high-mass sources. The two panels in each case refer to the use of LOFAR and SKA for the 21 cm power spectrum measurement. The dashed lines show the location of the 'true' values of the parameters. The green contours show the 1σ and 2σ constraints when only 21 cm power spectrum data is used. Contours in other colours show constraints obtained when the [C II]−21cm cross power spectrum data is added to the analysis.

proof of concept. None the less, some simple radiative transfer models in the literature do suggest that Lyman-continuum photons are able to escape from a narrow range of halo masses (Ferrara & Loeb 2013). Our parametrization describes this possibility.

To assess the capability of observations to constrain the parameters $M_{\rm esc}$ and $N_\gamma^{\rm LyC}$, we create mock power spectra with experimental uncertainties and derive posterior probability distributions for these parameters using Markov Chain Monte Carlo (MCMC). This approach is similar to that considered, for instance, for 21 cm experiments by Greig & Mesinger (2015). We consider two mock observations of the 21 cm power spectrum and the [C II]−21cm cross power spectrum. In one of these mocks, our two parameters have values $M_{\rm esc} = 5.56 \times 10^8$ M$_\odot$ and $N_\gamma^{\rm LyC} = 3.5$. This corresponds to the power spectra shown in Fig. 3. The associated uncertainties are also those shown in Fig. 3. For the second mock observation, the mock measurements and associated errors are the power spectra shown in Fig. 4. This mock data has $M_{\rm esc} = 10^{11}$ M$_\odot$ and $N_\gamma^{\rm LyC} = 14$. As the shot noise dominates the total power, we only fit the clustering power spectrum in this exercise.

For each of the mock data sets, we infer the posterior distributions for $M_{\rm esc}$ and $N_\gamma^{\rm LyC}$ by writing a Gaussian likelihood for the data as

$$\log \mathcal{L}(\Delta^2 | M_{\rm esc}, N_\gamma^{\rm LyC}) \propto -\frac{1}{2}\sum_i \log\left(2\pi\sigma^2(k_i)\right) - \sum_i \frac{(\Delta^2_{\rm mock}(k_i) - \Delta^2_{\rm model}(k_i, M_{\rm esc}, N_\gamma^{\rm LyC}))^2}{2\sigma^2(k_i)}, \quad (32)$$

where Δ^2 denotes the power spectrum or the cross power spectrum, as the case may be, the index i runs over the k bins, and σ is the error on the mock observation at wavenumber k_i, estimated for various experiments following the procedure described in Sections 5.1 and 5.2. We then explore the capability of our model to identify the parameters used to create the mock data, by inferring the values of these parameters in a Bayesian fashion. We use MCMC to sample the posterior distributions of the parameters, using a modified version of the 21 cm inference code 21CMMC (Greig & Mesinger 2015) to derive distributions for the parameters $M_{\rm esc}$ and $N_{\rm min}^{\rm LyC}$ assuming wide, uniform priors. For given values of the parameters, we compute $\Delta^2_{\rm model}$ by first running our simulation (as described in Section 2 and Section 4; with the power spectrum and cross power spectrum as defined in equations 8 and 17) over a grid of points in the parameter space and then linearly interpolating between the values of the likelihood to get it at an arbitrary parameter value. Our grid of models has 399 simulations. It spans 19 values of $N_{\rm min}^{\rm LyC}$ and 21 values of $M_{\rm esc}$.

The resultant posterior joint probability distributions are shown in Fig. 7. Panels in the top row describe the low-mass reionization scenario, and those in the bottom row describe the high-mass reionization scenario. The two panels in each case refer to the use of LOFAR and SKA for the 21 cm power spectrum measurement. The dashed lines show the location of the 'true' values of the parameters, which were used to produce the mock data. The green contours show the 1σ and 2σ constraints when only 21 cm power spectrum data is used. In this case, there is a strong degeneracy in the two parameters in the low-mass reionization scenario. This degeneracy persists in the high-mass case, although its magnitude is considerably reduced. Constraints in the high-mass case are good even with the 21 cm data alone, as the power spectrum has an enhanced amplitude in this case, which allows for a high-signal-to-noise measurement. Contours in other colours in Fig. 7 show constraints obtained when the [C II]−21cm cross power spectrum data is added to the analysis. We find that this considerably improves the constraints for the Stage II [C II] experiment. With data from 1000 and 5000 h of the Stage II experiment, the improvement in 1σ constraints on $M_{\rm esc}$ relative to 21 cm measurements is by factors of 3 and 10, respectively. The improvement is of a comparable magnitude in the high-mass case. The constraints also show a modest improvement when SKA measurements are considered instead of LOFAR. Due to low signal to noise, 1500 h data from CONCERTO do not result in a significant improvement in the constraints.

7 CONCLUSIONS

We have outlined the prospects of intensity mapping the epoch of reionization using the redshifted 21 cm line and the [C II] emission line from high-redshift galaxies. We have modelled the galaxy line emissions using a SAM. Using a high dynamic range cosmological simulation, we found that on large scales of $\gtrsim$60 cMpc h^{-1} at redshift $z = 6$ the spherically averaged power spectrum of the [C II] line emission have values of $\Delta^2 \sim 10^5$ (Jy sr^{-1})^2 at $k \sim 0.2\ h$ cMpc^{-1}. This value reduces to about 10^3 (Jy sr^{-1})^2 at $z \sim 9$.

We find that the [C II] power spectrum predicted in our model should be detectable with the CONCERTO experiment up to $z \sim 8$ with a signal-to-noise ratio of $\gtrsim$1 at $k = 0.2\ h$ cMpc^{-1}. A Stage-II experiment with five times better sensitivity than CONCERTO should be able to detect the [C II] power spectrum at even higher redshifts. The cross power spectrum of the [C II] and coeval 21 cm signal from the epoch of reionization would be valuable in many ways. The scale at which this cross power spectrum changes sign can contain the average size of ionized regions, at least when the sources of reionization coincide with the galaxies that produce the [C II] signal. A detection of this cross power spectrum could help in the removal of low-redshift foregrounds from the 21 cm data. The cross power spectrum will also provide constraints on important astrophysical parameters. We have investigated the capability by analysing mock 21 cm power spectrum data and [C II]−21cm cross power spectrum data in a Bayesian way to derive constraints under various experimental assumptions. We find that [C II]−21cm correlation measurements can improve constraints on the mass of reionization sources by factors of 3–10 beyond constraints from 21 cm experiments alone.

ACKNOWLEDGEMENTS

We acknowledge helpful discussions with Dongwoo Chung, Andrea Pallottini, and Ewald Puchwein, and also thank the anonymous referee for their comments. Support by ERC Advanced Grant 320596 'The Emergence of Structure During the Epoch of Reionization' is gratefully acknowledged. We acknowledge PRACE for awarding us access to the Curie supercomputer, based in France at the Trés Grand Centre de Calcul (TGCC). GL acknowledges financial support from the 'Programme National de Cosmologie and Galaxies' (PNCG) funded by CNRS/INSU-IN2P3-INP, CEA and CNES, France. This work used the DiRAC Data Centric system at Durham University, operated by the Institute for Computational Cosmology on behalf of the STFC DiRAC HPC Facility (www.dirac.ac.uk). This equipment was funded by BIS National E-infrastructure capital grant ST/K00042X/1, STFC capital grants ST/H008519/1 and ST/K00087X/1, STFC DiRAC Operations grant ST/K003267/1 and Durham University. DiRAC is part of the National E-Infrastructure.

REFERENCES

Adam R. et al., 2018, A&A, 609, A115
Barkana R. Loeb A., 2001, Phys. Rep., 349, 125
Becker G. D. Bolton J. S. Haehnelt M. G. Sargent W. L. W., 2011, MNRAS, 410, 1096
Becker G. D. Bolton J. S. Madau P. Pettini M. Ryan-Weber E. V. Venemans B. P., 2015, MNRAS, 447, 3402
Bolton J. S. Puchwein E. Sijacki D. Haehnelt M. G. Kim T.-S. Meiksin A. Regan J. A. Viel M., 2017, MNRAS, 464, 897
Boutsia K. et al., 2011, ApJ, 736, 41
Bowman J. D. et al., 2013, Publ. Astron. Soc. Aust., 30, e031
Bradač M. et al., 2017, ApJ, 836, L2
Carilli C. L., 2011, ApJ, 730, L30
Carilli C. L. Walter F., 2013, ARA&A, 51, 105
Carniani S. et al., 2017, A&A, 605, A42
Chang T.-C. Pen U.-L. Bandura K. Peterson J. B., 2010, Nature, 466, 463
Chardin J. Haehnelt M. G. Aubert D. Puchwein E., 2015, MNRAS, 453, 2943
Choudhury T. R. Haehnelt M. G. Regan J., 2009, MNRAS, 394, 960
Cooray A. et al., 2016, preprint (astro-ph/1602.05178)
Cousin M. Lagache G. Bethermin M. Blaizot J. Guiderdoni B., 2015, A&A, 575, A32
Cousin M. Buat V. Boissier S. Bethermin M. Roehlly Y. Génois M., 2016, A&A, 589, A109
Crites A. T. et al., 2014, in Holland W. S., Zmuidzinas J., eds, Proc. SPIE Conf. Ser., Vol. 9153, Millimeter, Submillimeter, and Far-Infrared Detectors and Instrumentation for Astronomy VII. SPIE, Bellingham, p. 91531W
D'Aloisio A. Upton Sanderbeck P. R. McQuinn M. Trac H. Shapiro P. R., 2017, MNRAS, 468, 4691

Davies F. B. Furlanetto S. R., 2016, MNRAS, 460, 1328
DeBoer D. R. et al., 2017, PASP, 129, 045001
Doré O. et al., 2014, preprint (astro-ph/1412.4872)
Doré O. et al., 2016, preprint (astro-ph/1606.07039)
Fan X. et al., 2006, AJ, 132, 117
Feng C. Cooray A. Keating B., 2017, ApJ, 846, 21
Ferland G. J. et al., 2017, Rev. Mex. Astron. Astrofis., 53, 385
Ferrara A. Loeb A., 2013, MNRAS, 431, 2826
Finkelstein S. L., 2016, Publ. Astron. Soc. Aust., 33, e037
Finlator K. Oppenheimer B. D. Davé R. Zackrisson E. Thompson R. Huang S., 2016, MNRAS, 459, 2299
Fonseca J. Silva M. B. Santos M. G. Cooray A., 2017, MNRAS, 464, 1948
Furlanetto S. R. Zaldarriaga M. Hernquist L., 2004a, ApJ, 613, 1
Furlanetto S. R. Zaldarriaga M. Hernquist L., 2004b, ApJ, 613, 16
Ghara R. Choudhury T. R. Datta K. K., 2016, MNRAS, 460, 827
Giallongo E. et al., 2015, A&A, 578, A83
Gong Y. Cooray A. Silva M. B. Santos M. G. Lubin P., 2011, ApJ, 728, L46
Gong Y. Cooray A. Silva M. Santos M. G. Bock J. Bradford C. M. Zemcov M., 2012, ApJ, 745, 49
Gong Y. Cooray A. Santos M. G., 2013, ApJ, 768, 130
Grazian A. et al., 2016, A&A, 585, A48
Greig B. Mesinger A., 2015, MNRAS, 449, 4246
Haardt F. Madau P., 2012, ApJ, 746, 125
Hill G. J. et al., 2008, in Kodama T. Yamada T. Aoki K., eds, ASP Conf. Ser. , Vol. 399. Panoramic Views of Galaxy Formation and Evolution. Astron. Soc. Pac., San Francisco, p. 115
Ikeuchi S. Ostriker J. P., 1986, ApJ, 301, 522
Japelj J. et al., 2017, MNRAS, 468, 389
Katz N. Weinberg D. H. Hernquist L., 1996, ApJS, 105, 19
Keating G. K. Marrone D. P. Bower G. C. Leitch E. Carlstrom J. E. DeBoer D. R., 2016, ApJ, 830, 34
Khaire V. Srianand R. Choudhury T. R. Gaikwad P., 2016, MNRAS, 457, 4051
Knudsen K. K. Richard J. Kneib J.-P. Jauzac M. Clément B. Drouart G. Egami E. Lindroos L., 2016, MNRAS, 462, L6
Kulkarni G. Choudhury T. R. Puchwein E. Haehnelt M. G., 2016, MNRAS, 463, 2583
Kulkarni G. Choudhury T. R. Puchwein E. Haehnelt M. G., 2017, MNRAS, 469, 4283
Lagache G., 2018, preprint (astro-ph/1801.08054)
Lagache G. Cousin M. Chatzikos M., 2017, A&A, 609, A130
Lidz A. Furlanetto S. R. Oh S. P. Aguirre J. Chang T.-C. Doré O. Pritchard J. R., 2011, ApJ, 741, 70
Livermore R. C. Finkelstein S. L. Lotz J. M., 2017, ApJ, 835, 113
Li T. Y. Wechsler R. H. Devaraj K. Church S. E., 2016, ApJ, 817, 169
Madau P. Haardt F., 2015, ApJ, 813, L8
Mesinger A. Furlanetto S. Cen R., 2011, MNRAS, 411, 955
Micheva G. Iwata I. Inoue A. K. Matsuda Y. Yamada T. Hayashino T., 2017, MNRAS, 465, 316
Mostardi R. E. Shapley A. E. Steidel C. C. Trainor R. F. Reddy N. A. Siana B., 2015, ApJ, 810, 107
Obreschkow D. Croton D. De Lucia G. Khochfar S. Rawlings S., 2009, ApJ, 698, 1467
Oesch P. A. Bouwens R. J. Illingworth G. D. Franx M. Ammons S. M. van Dokkum P. G. Trenti M. Labbé I., 2015, ApJ, 808, 104
Oesch P. A. et al., 2016, ApJ, 819, 129
Ota K. et al., 2017, ApJ, 844, 85
Parsons A. Pober J. McQuinn M. Jacobs D. Aguirre J., 2012, ApJ, 753, 81
Pentericci L. et al., 2016, ApJ, 829, L11
Planck Collaboration XVI, 2014, A&A, 571, A16
Planck Collaboration XLVII, 2016, A&A, 596, A108
Pober J. C. et al., 2014, ApJ, 782, 66
Puchwein E. Haardt F. Haehnelt M. G. Madau P., 2019, MNRAS, 485, 47
Pullen A. R. Doré O. Bock J., 2014, ApJ, 786, 111
Pullen A. R. Serra P. Chang T.-C. Doré O. Ho S., 2018, MNRAS, 478, 1911
Robertson B. E. Ellis R. S. Furlanetto S. R. Dunlop J. S., 2015, ApJ, 802, L19
Serra P. Doré O. Lagache G., 2016, ApJ, 833, 153
Siana B. et al., 2015, ApJ, 804, 17
Silva M. B. Santos M. G. Gong Y. Cooray A. Bock J., 2013, ApJ, 763, 132
Silva M. Santos M. G. Cooray A. Gong Y., 2015, ApJ, 806, 209
Springel V., 2005, MNRAS, 364, 1105
Springel V. Yoshida N. White S. D. M., 2001, New Astron., 6, 79
Strandet M. L. et al., 2017, ApJ, 842, L15
Suginohara M. Suginohara T. Spergel D. N., 1999, ApJ, 512, 547
Thompson A. R. Moran J. M. Swenson G. W., 2001, Interferometry and Synthesis in Radio Astronomy. Wiley, New York
Tingay S. J. et al., 2013, Publ. Astron. Soc. Aust., 30, e007
van Haarlem M. P. et al., 2013, A&A, 556, A2
Vanzella E. et al., 2010, ApJ, 725, 1011
Viel M. Haehnelt M. G. Springel V., 2004, MNRAS, 354, 684
Visbal E. Loeb A., 2010, J. Cosmol. Astropart. Phys., 11, 016
Visbal E. Trac H. Loeb A., 2011, J. Cosmol. Astropart. Phys., 8, 010
Yue B. Ferrara A. Pallottini A. Gallerani S. Vallini L., 2015, MNRAS, 450, 3829

This paper has been typeset from a TEX/LATEX file prepared by the author.